Insights into Adsorption of NH3 on HKUST-1 Metal–Organic Framework: A Multitechnique Approach

(Article begins on next page)

06 October 2024

Insights into adsorption of NH₃ on HKUST-1 metal-organic framework: a multi-technique approach

by
Elisa Borfecchia, Sara Maurelli, Diego Gianolio, Elena Groppo, Mario Chiesa,
Francesca Bonino and Carlo Lamberti

Insights into adsorption of NH$_3$ on HKUST-1 metal-organic framework: a multi-technique approach

Elisa Borfecchia,[1] Sara Maurelli,[1] Diego Gianolio,[2] Elena Groppo,[1] Mario Chiesa,[1] Francesca Bonino[1,] and Carlo Lamberti[1]*

[1]Department of Chemistry, NIS Centre of Excellence, and INSTM reference center, University of Turin, Via P. Giuria 7, I-10125 and Via Quarello 11, I-10135, Torino, Italy

[2] Diamond Light Source Ltd, Harwell Science and Innovation Campus, OX11 0DE, Didcot (UK)

Abstract We report a careful characterization of the interaction of NH$_3$ with the Cu(II) sites of the [Cu$_2$C$_4$O$_8$] paddle-wheel cornerstone of the HKUST-1 metallorganic framework, also known as Cu$_3$(BTC)$_2$. The general picture emerging from combiningXRPD, EXAFS, XANES, Mid- and Far-IR, DRUV-Vis, and EPR techniques is that the presence of traces of water has relevant consequences on effect that interaction of ammonia has on the MOF framework. NH$_3$ adsorption on the dry system results in a strong chemisorption on Cu(II) sites that distorts the framework, keeping the crystallinity of the material. Perturbation observed upon NH$_3$ absorption is analogue to that one observed in the case of H$_2$O, but noticeably enhanced. When the adsorption of ammonia occurs in humid conditions a time dependent, much deeper modification of the system is observed by all the considered techniques. On a methodological ground, it is worth noticing that we used the optimization of XANES spectra to validate the bond distance obtained by EXAFS.

Keywords: NH$_3$ capture; HKUST-1; Cu$_3$(BTC)$_2$ MOF; in situ spectroscopies; framework stability; NH$_3$/H$_2$O co-adsorption

1. Introduction

Metal Organic Frameworks (MOFs) are crystalline nanoporous materials comprised of two basic structural building units: transition metal ions, or small metal-containing clusters, and connecting polyfunctional organic ligands such as di- or tri-carboxylic acids.[1-8] These materials are characterized by a crystalline three-dimensional structure, with very high pore volume and surface area. This hybrid architecture opens the possibility to design and synthesize a great variety of new porous materials, which are in principle able to display novel functionalities that are potentially exploitable for a number of applications in catalysis,[9-19] gas sorption, storage and separation by selective adsorption.[20 21-31]

Among the several hundred of different MOF structures, Cu$_3$(BTC)$_2$(H$_2$O)$_3$ (BTC = benzene 1,3,5-tricarboxylate), also known as HKUST-1,[32] is one of the most investigated one and among the first commercially available representatives of this class of organic-inorganic hybrid materials, featuring specific adsorption[33-36], magnetic,[37] and catalytic properties.[38] HKUST-1 is characterized by so-called paddle-wheel units formed by four carboxylate groups coordinating two antiferromagnetically coupled Cu(II) ions. The Cu(II) dimers are connected by the BTC linker molecules to form a three-dimensional porous network; water molecules are weakly bound to the residual axial binding site of the Cu(II) ions. These axial water molecules can be easily removed from the Cu(II) dimers by heating at moderate temperature in vacuum to form structurally well-defined accessible Lewis acid copper sites available for chemisorptions of molecules having basic

character.[35,36] In particular, the present contribution is devoted to study the strong adsorption of ammonia basic molecule at room temperature.[39-43]

Ammonia capture is a problem that has some technological relevance. As an example, the biogas produced from anaerobic digestion of bio-waste (*i.e.* animal manure) is mainly composed by methane and carbon dioxide, but also contains some impurity gases, such as ammonia, that has to be removed from the biogas prior to its energy application.[44] Nature has developed complex enzymes able to selectively bind NH_3 molecules;[45] HKUST-1 porous MOF can be considered as a promising synthetic counterpart.[32,39-42,46] The potential of HKUST-1 in ammonia removal from contaminated air streams was reported many years ago by Chui and co-workers[32]. The reaction of ammonia with the individual building blocks of $Cu_3(BTC)_2$, i.e., Cu(II) ion and BTC, is well known. In aqueous solution, Cu(II) ion, in the presence of limited ammonia, is initially converted to $Cu(OH)_2$; however, copious amounts of ammonia eventually yield $[Cu(NH_3)_4]^{2+}$. Carboxylic acids initially form the ammonium salt which, with sufficient heating, can be pyrolized to their corresponding amides. Peterson et al. [39] states that HKUST-1 reacts with ammonia to form a presumed diammine-copper(II) complex under dry conditions and, under humid conditions, a $Cu(OH)_2$ species and $(NH_4)_3BTC$. Nitrogen adsorption, XRPD, and NMR testing of fresh and exhausted samples all provided evidence for the permanent loss of structure and/or porosity, with samples challenged with ammonia under humid conditions undergoing the largest change. Although the porosity of the material is destroyed, the resulting capacity of the exhausted samples for ammonia is indicative of an extended reactive network consistent with that of the copper(II) complex products.

Herein, we present new details on the adsorption properties of HKUST-1 towards ammonia by applying a multitude of characterization techniques (XRPD, XAFS, IR, DR-UV-Visible-NIR and EPR).

2. Experimental Section
2.1. Sample Preparation

HKUST-1 sample was purchased by Sigma - Aldrich. The dehydrated form of HKUST-1 has been obtained upon activation in high vacuum for 1h at 423 K. Rehydration of the samples was obtained upon contacting the powder with the vapor pressure of water at room temperature: these conditions are significantly milder than those experienced by Kuesgen et al.[47] where HKUST-1 was immersed in de-ionized water and heated to 323 K for 24 h. As prepared (rehydrated) and dehydrated samples were exposed to an ammonia equilibrium pressure of 60 mbar. The adsorption of both water and ammonia was carried out at room temperature. EXAFS spectroscopy testify that adsorption of water vapor pressure and of 60 mbar of NH_3 results in a 1:1 Cu:adsorbate ratio. A large amount of sample was subjected to the same treatment and further separated in different fractions, which were measured by XRPD, XAFS, DR-UV-Visible and IR. This method guarantees that the same sample is measured by different techniques.

2.2. Structural characterization: XRPD and XAFS
2.2.1 XRPD measurements. X-ray Powder Diffraction (XRPD) patterns have been collected with a PW3050/60 X'Pert PRO MPD diffractometer from PANalytical working in Debye–Scherrer geometry, using as source the high power ceramic tube PW3373/10 LFF with a Cu anode equipped with Ni filter to attenuate Kb and focused by X-ray mirror PW3152/63. Scattered photons have been collected by a RTMS (Real Time Multiple Strip) X'celerator detector. The samples have been measured as powders inside a 0.8 mm boronsilicate capillary filled in a glove-box and sealed in inert atmosphere, in order to prevent contamination from moisture.

2.2.2 XAFS measurements. X-ray absorption experiments, at the Cu K-edge (8979 eV), were performed at the BM26B beamline of the ESRF facility (Grenoble, F).[48,49] The white beam was monochromatized using a Si(111) double crystal; harmonic rejection was performed by detuning the crystals at 20% of the rocking curve. The samples were prepared in the form of a pellet, with the

thickness optimized to obtain an edge jump of ca. 1, and an absolute μx of ca. 1.5. The same pellet was activated and successively treated with NH_3 inside a devoted glass cell equipped with kapton windows, which allows to perform *in situ* measurements.[50] XAS measurements were performed in transmission mode, using two ionization chambers to monitor the intensity of incident I_0 and transmitted I_1 beams. The chambers were filled with 1 atm of mixed gases (N_2 15%, He 85% for I_0 and N_2 70%, He 30% for I_1), resulting in 10% and 50% of absorption, respectively. Energy calibration was checked using a Cu metal foil positioned after the second ionization chamber (I_1) and measured using a third ionization chamber (I_2), as described elsewhere.[51] The pre-edge region of the XAS spectrum was acquired with an energy step of 10 eV and an integration time of 1 s/point. The edge region was collected using an energy step of 0.2 eV and an integration time of 5 s/point. The EXAFS part of the spectra was collected with a variable sampling step in energy, resulting in $\Delta k = 0.05$ Å^{-1}, up to 18 Å^{-1}, with an integration time that linearly increases with k from 5 to 25 s/point to account for the low signal-to-noise ratio at high k values. The extraction of the $\chi(k)$ function was performed using Athena program.[52] For each sample, four consecutive EXAFS spectra have been collected and corresponding k^3-weighted $\chi(k)$ functions have been averaged before data analysis, as described elsewhere, [53] and Fourier transformed in the $\Delta k = 2.0 - 16.0$ Å^{-1} range. The fits of the EXAFS spectra measured for the as prepared, activated and activated + NH_3 HKUST-1 were performed in R-space in the $\Delta R = 1.0 - 5.0$ Å range, resulting in 35 independent points ($2\Delta k\Delta R/\pi > 35$). Due to the complexity of the structure,[36,54] more than 50 single scattering (SS) and multiple scattering (MS) paths were included in the fit. To limit the number of optimized variables, all paths have been optimized with the same amplitude factor (S_0^2) and with the same energy shift parameter (ΔE). Phases and amplitudes have been calculated by FEFF6 code[55] adopting as input the structure obtained from a previous XRD refinement.[32,36]

XANES spectra of the hydrated MOF have been simulated using FEFF8.4 code,[56] adopting as input geometry the XRPD structure[32] and cutting a cluster centered on one of the Cu atoms with a radius of 6 Å around it. For a further improvement of the simulations, an optimization of geometrical parameters was performed exploiting Fitit software. [57] The simulation of the dehydrated sample was obtained removing the water molecules from the previous cluster, while for the sample in interaction with ammonia the H_2O molecules were substituted by two NH_3 ones. In both cases the structure was optimized to match the experimental spectrum as described for the hydrated case.

In all cases, calculations for the absorption spectra and densities of states have been done using the muffin-tin potential and the Hedin-Lundqvist exchange correlation, taking care of the presence of a core hole in a self-consistency scheme (for the self consistent calculations it has been used a radius of 4 Å). To take into account the experimental broadening, an imaginary potential $V_i = 1.0$ eV has been introduced. Although quadrupole transitions are much weaker than the dipole ones, their contribution has been considered in calculations.

2.3. IR spectroscopy

IR spectra have been collected in both Mid-IR region (3800 – 400 cm^{-1}) and Far-IR region (600 – 100 cm^{-1}). IR spectra in the Mid-IR region have been collected in ATR mode, by using a Bruker Alpha instrument equipped with an ATR accessory (diamond crystal), and placed inside the glove-box; the spectra have been collected at a resolution of 2 cm^{-1}. It is worth noticing that ATR acquisition mode allows to collect IR spectra on pure samples in the powdered form without necessity to make a pellet using KBr as diluent (which unavoidably contains some water). This is an advantage when handling samples sensitive to moisture, as in our case. Far-IR spectra have been collected at a resolution of 2 cm^{-1} on a Bruker Vertex 70 instrument, equipped with a Si beam splitter and a Far-IR DTGS detector. The samples have been diluted in paraffin.

2.4. UV-Visible-NIR spectroscopy

UV-Vis-NIR spectra have been collected in Diffuse Reflectance (DR) mode on a Cary5000 Varian spectrophotometer equipped with a reflectance sphere. All the samples have been measured in the powdered form inside a home-made cell having an optical bulb (suprasil quartz) and allowing to perform measurements in controlled atmosphere.

2.5. EPR Measurements

CW EPR spectra were recorded on a Bruker EMX spectrometer operating at X-band frequencies and equipped with a cylindrical cavity operating at a 100 kHz field modulation. The spectra have been recorded at 10 mW microwave power. The spectra processing was performed with software provided by Bruker, while for computer simulation the *EPRsim32* program was used.[58]

Pulse EPR experiments were performed on an ELEXYS 580 Bruker spectrometer (at microwave frequency 9.76 GHz) equipped with a liquid-helium cryostat from Oxford Inc. All experiments were performed at 10 K. The magnetic field was measured with a Bruker ER035M NMR Gaussmeter.

Electron-spin-echo (ESE) detected EPR experiments were carried out with the pulse sequence: $\pi/2-\tau-\pi-\tau-echo$, with microwave pulse lengths $t_{\pi/2} = 16$ ns and $t_{\pi/2} = 32$ ns and a τ value of 200 ns. Hyperfine Sublevel Correlation (HYSCORE) experiments[59] were carried out with the pulse sequence $\pi/2-\tau-\pi/2-t_1-\pi-t_2-\pi/2-\tau-echo$ with microwave pulse length $t_{\pi/2} = 16$ ns and $t_\pi = 16$ ns. The time intervals t_1 and t_2 were varied in steps of 8 ns starting from 100 ns to 3300 ns. Two different τ values were chosen ($\tau = 96$ ns and 172 ns). An eight-step phase cycle was used to eliminate unwanted echoes.

The time traces of the HYSCORE spectra were baseline corrected with a third-order polynomial, apodized with a Hamming window and zero filled. After two-dimensional Fourier transformation, the absolute value spectra were calculated. The spectra were added for the different τ values in order to eliminate blind-spot effects. The HYSCORE spectra were simulated using *EasySpin* package.[60]

3. Results and discussion

3.1. XRPD analysis. The XRPD pattern of as-synthetized hydrated HKUST-1 (blue curve in Figure 1) confirms the crystalline nature of the sample and the absence of any extra-phase. [36] Upon dosage of ammonia on hydrated HKUST-1 the XRPD pattern is strongly modified (orange curve in Figure 1), indicating a significant distortion of the lattice, which however does not undergo a complete amorphization. After prolonged exposure time, a further modification of the diffraction features, along with an overall broadening of the peaks, is observed (Figure 1, purple curve).[39]

The XRPD pattern of the activated sample (pink curve in Figure 1) was previously reported by Prestipino *et al.* [36]. This pattern shows an overall slight shift of the diffraction peaks towards higher θ-values if compared to that of the as-prepared material; this observation is compatible with a global contraction of the bond lengths induced by the activation process. Moreover, the dehydration induces a strong intensity enhancement of a diffraction peak in the very low-θ region, around 6.7°. Surprisingly, if pure dry ammonia is dosed on the activated material, the diffraction pattern (light green curve in Figure 1) is much less perturbed than that obtained by dosing ammonia on the hydrated sample. Nevertheless, comparing this pattern with the one measured for the activated MOF, a slight shift in the peaks positions towards shorter θ values is observed, as well as small variations in their relative intensities. The intense peak around 6.7° already observed for the activated material is maintained after interaction with dry NH_3. The main difference with respect to the pattern of the activated sample is the appearance of a peak around 5.8°, which was not present at all in the pattern of the activated material. Therefore it should be concluded that HKUST-1 framework is only slightly perturbed upon NH3 adsorption and goes back to a situation similar to that characteristic of hydrated material, with a slight generalized lengthening of the bond distances. Finally, the XRPD pattern does not change when H_2O is dosed on the sample pre-contacted with

NH_3 (Figure 1, dark green curve). The XRPD data shown in Figure 1 demonstrates that NH_3 alone affects the crystalline structure of the dehydrated HKUST-1 only very slightly, whereas in combination with H_2O it causes a drastic change in the structure, up to the complete amorphization of the sample. However, the effect is observed only when H_2O is dosed first, and NH_3 later.

The quality of the XRPD data shown in Figure 1 is not enough to allow a structure refinement. In order to gain information on the local environment around copper centres in absence and in presence of ammonia we used Cu K-edge EXAFS spectroscopy.
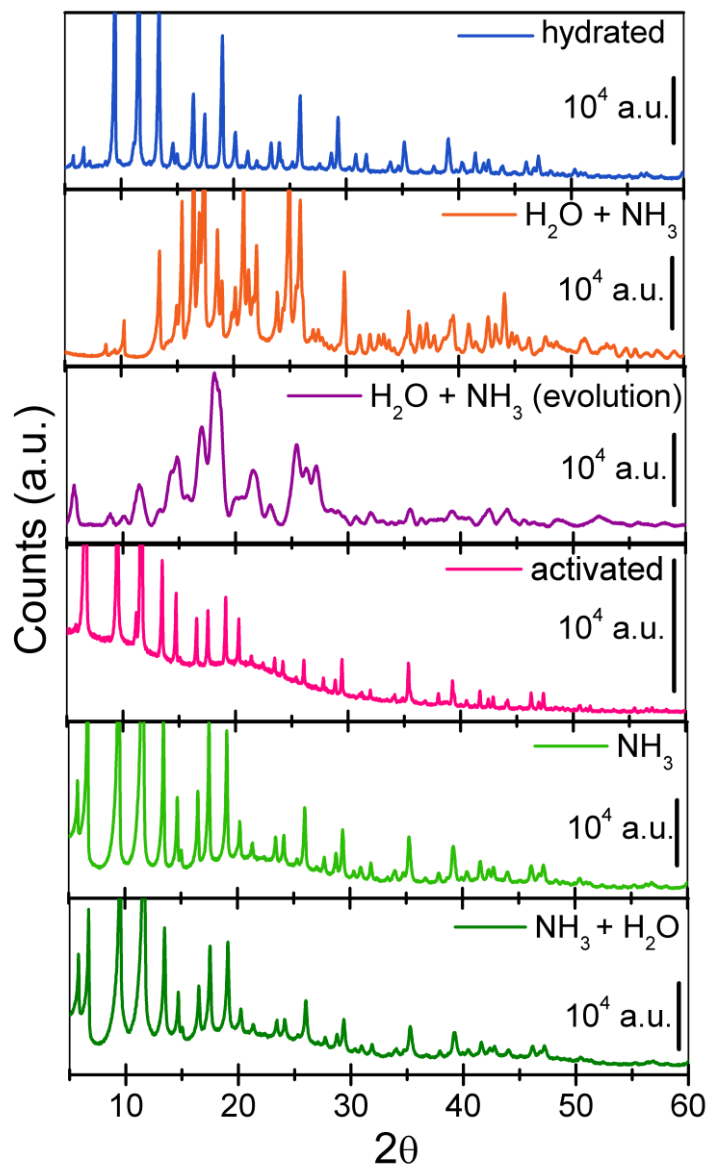

Figure 1. XRPD patterns of HKUST-1 in different conditions: as-prepared (hydrated, blue line), after dosage of ammonia on a sample previously contacted with water vapor pressure (orange line), and its evolution after prolonged exposure time in such conditions (purple line), activated sample (pink line, adapted from Prestipino et al [36]), after pure dry ammonia dosage on the activated sample (light green line), and after contacting with water vapor pressure the sample previously exposed to ammonia in dry conditions (dark green line).

3.2. XAS analysis

3.2.1 XANES Spectroscopy. Investigation of the XANES region of the X-ray absorption spectrum can provide detailed information on both the oxidation state and the coordination symmetry of the absorber atom, and was successfully applied in the structural characterization of

several Cu-containing materials.[36,51,61-72] In Figure 2a, top panel, are reported the experimental XANES spectra of HKUST-1 as-prepared (hydrated sample, blue solid line), after activation at 453 K (dehydrated sample, pink solid line) and upon contact with 60 mbar of ammonia at room temperature (green solid line). As pointed out in a previous work,[36] the XANES spectra of the as prepared and dehydrated sample are typical of Cu(II) species, showing the edge jump at 8990 eV and two characteristic pre-edge peaks at ca. 8976 eV and ca. 8986 eV, labelled as **(1)** and **(2),** respectively, in Figure 2a, and separately reported in the insets of the same Figure. Feature **(1)** is assigned to the very weak $1s \rightarrow 3d$ quadupolar transition, while the shoulder **(2)** appearing along the white line profile is related to the dipolar shakedown $1s \rightarrow 4p$ transition. The simulation of the spectrum of the hydrated material was performed starting from the XRPD structure[32] and optimizing five structural parameters: (i) the Cu-Cu and (ii) Cu-H_2O bond length, the distance between the Cu atom and the trimesic acid carboxyl groups with a separate optimization of (iii) Cu-O1 and of (iv) Cu-C and Cu-O2 distances (optimized in a correlated way to use only one free parameter) and (v) a general overall contraction or elongation of all the other distances ($R_{XANES} = \alpha R_{XRPD}$).[73] Vide infra Figure 3a for the atom notation. The variations in the simulated spectrum introduced by the geometrical distortions have been monitored by using the FitIt software. In conclusion it has been observed that a variation of Cu-Cu distance reflected in very slight changes in the XANES features, the Cu-H_2O distance influences the intensity and partially the position in energy of the pre-edge feature **(2)**, the carbonyl groups distances and a possible overall contraction or expansion strongly influence both the intensity and the position of the white line and the shape of the multiple scattering features at higher energies. In the case of the hydrated sample, the best agreement between the simulated curve and experimental data was obtained with a slight shortening of Cu-H_2O distance, an elongation of 0.05 Å of both Cu-O1 and the constrained Cu-C and Cu-O2 distances, corresponding to a shift along the bond axis of the carbonyl groups and a slight general contraction of all other distances. Upon water removal, no shift in the absorption edge is observed, providing an evidence that no change in oxidation state of the Cu centre occurs. However, the XANES spectrum of the activated sample shows: i) a decrease of the white line intensity, and ii) an increase in the intensity of feature **(2)**, that appears more as a well separated band than as a white line shoulder. The simulation of the XANES spectrum for the activated sample was performed with the same method previously described for the hydrated sample removing the atoms of the two water molecules, resulting in an optimization with four parameters only. Even without a structural optimization, in the simulated spectra it has been observed the same trend noticed on the experimental curves where the decrease of the white line intensity is correlated to the lower coordination number, and the increase of the intensity of feature **(2)** is ascribable to a lower symmetry of the Cu(II) species. In the simulated curves this trend is less evident probably because a full description of the asymmetric distortion undergone by the Cu species in the activated sample would require a too high number of parameters to be optimized. The optimization of the bond distances resulted in a slight contraction of the distances between the absorbing Cu atom and carbonyl groups and all other distances, in agreement with the results found by EXAFS fit (see Section 3.2.2 and Table 1). The XANES spectrum of the activated sample after the interaction with NH_3 evidences an additional increase in the intensity and a slight blue-shift of the dipole band **(2)** assigned to the 1s $\rightarrow$ 4p transition. Moreover, a new pre-edge peak is observed at ca. 8983 eV. Despite the edge position is not modified respect to the as prepared and activated samples (no change in oxidation state of the metal), the white line is modified towards a more structured appearance, and seems to return towards the shape observed in the case of the hydrated sample. The simulation of the spectrum for the sample after interaction with NH_3 was performed following the same method adopted for the hydrated material and substituting the water molecules with two NH_3 molecules. After the optimization of the geometrical parameters it has been observed that an increasing of the intensity of the pre-edge feature **(2)** is proportional to the the Cu-NH_3 distance which was optimized at 2.3 Å with a considerable elongation with respect to the previous position of the water molecules. Moreover a splitting of the white line feature, even if less evident with

respect to the experimental spectra, has been observed after a distortion of carbonyl groups simulated by a slight elongation of Cu-O1 distances but a severe shortening of both Cu-C and Cu-O2 and all other distances. It is worth noticing that the deformation introduced to simulate the XANES spectra is in agreement with the results of the EXAFS fit.
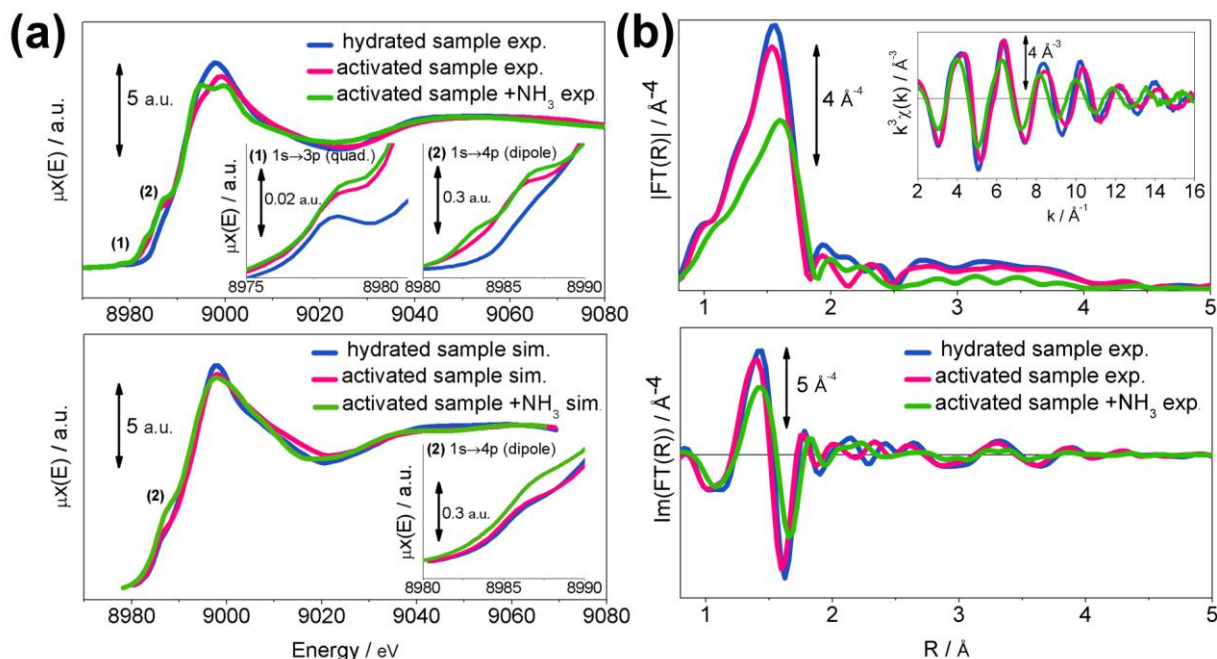

Figure 2. Part (a): Experimental (top panel) and simulated (bottom panel) XANES spectra of HKUST-1 as prepared (blue line), activated (pink line) and activated + NH$_3$ (green line). The insets report magnifications of the $1s \rightarrow 3d$ quadupolar transition **(1)** and of the shakedown $1s \rightarrow 4p$ transition **(2)**. Part (b): Qualitative comparison between experimental EXAFS data for as prepared and activated HKUST-1, and for the activated sample upon contact with 50 mbar of ammonia. Modulus (top panel) and imaginary part (bottom panel) of the FT of the k^3-weighted χ(k) functions reported in the inset for the as prepared (blue line), activated (pink line) and activated + NH$_3$ (green line) sample. The inset in top part reports the corresponding k^3 χ(k) functions.

3.2.2 EXAFS Spectroscopy The quality of the EXAFS spectra, in terms of S/N ratio, can be checked in Figure 2b (inset in the top panel), where the extracted k$^3\chi$(k) functions are reported. EXAFS data analysis was performed up to k = 16 Å^{-1}, thus obtaining satisfactory structural information up to the third shell of atoms around the Cu absorber, i.e. up to atomic distances within a sphere with ca. 5 Å of radius. The corresponding k^3-weighted Fourier transformed functions, in the 2 – 16 Å^{-1} range, are shown in Figure 2b for both the moduli (top panel) and imaginary parts (bottom panel). The three spectra are dominated by the first shell signal (at ca. 1.5 Å, not corrected in phase); contributions at longer distances are weaker, although the modulation of the imaginary part provides an evidence that the experimental signal still contains structural information. The spectrum of the activated sample (pink curves) is very similar to that of the as prepared sample (blue curves), and only a slight shift towards shorter R-values and a small decrease of the amplitude of the first shell signal is observed. The shift reveals an overall contraction of the bond distances after thermal activation, in agreement with XRD data, while the lower first shell intensity is with a consequence of the reduction of the Cu coordination number (loss of the water molecule coordinated to the Cu atom). The imaginary parts of the FT in the high-R region (R > 2.5 Å) are very similar, indicating that after thermal activation the framework of HKUST-1 remains substantially unchanged at a long range, and only the first shell of the Cu-absorber is modified, as expected for dehydration.

The situation is drastically different for the activated sample in interaction with ammonia. The EXAFS spectrum is characterized by a first shell signal weaker and shifted towards longer bond

distances, if compared to that of the activated sample. In addition, oscillations of the Imm(FT) in the high-R range are noticeably damped in amplitude. The interpretation of this experimental behavior requires particular attention. The strong reduction of EXAFS signal might be intuitively ascribed to a great modification of the framework. However, the XRPD results (as well as IR and UV-Vis characterization, *vide infra*), demonstrate that only a slight structural rearrangement occurs upon NH_3 dosage in absence of water, coherent with the simple NH_3 coordination to the Cu metal centre after dehydration. As it will be discussed in details hereinafter, the lowering in the EXAFS signal amplitude can be explained with a phenomenon of destructive interference among some of the main EXAFS paths involved, already observed in the analysis of the as-such and activated samples, and further intensified after the NH_3 coordination.

A quantitative analysis of the EXAFS spectrum for the as-prepared sample has been performed starting from the cluster shown in Figure 3a, where the five shells of scatterer atoms giving the main contribution to the FT-transformed EXAFS signal are highlighted by different colored halos and the Cu atom acting as absorber is circled in red (Cu_{abs}). The first shell includes four equivalent oxygen atoms of the trimesic acid carboxyl groups in square planar geometry (O1) and the oxygen of the water molecule (O_{H2O}) directly coordinated to the Cu absorber. The main contributions at longer distance come from SS paths involving the second copper atom of the dimer (Cu) in front of the absorber, the four carbon atoms of the trimesic acid carboxyl groups (C), the four oxygen atoms coordinated to this second copper site (O2) and, finally, from Cu_{abs}–C–O1 MS paths. For all these scattering paths the distance and the Debye-Waller factor have been fitted independently. The remaining SS and MS were modeled describing length variation ΔR_i and Debye-Waller factor σ^2_i of the i-th path according to the following relations: $\Delta R_i = \alpha\ R^{eff}_i$ and $\sigma^2_i = \sigma^2\ (R^{eff}_i\ /R_{O1})^{1/2}$, i.e. considering the possibility of an overall isotropic contraction/dilatation of the distances (parameter α) and assuming a Debye-Waller factor increasing proportionally to the square root of the path effective length R^{eff}_i. This approach has already been used to limit the overall number of optimized parameters in systems where an high number of SS and MS path contribute significantly to the overall signal such as oxides[73-77] and MOFs.[31,54,78-84] Finally, a single ΔE and S_0^2 value common to all the paths have been fitted. The complete fitting model needed 14 independent parameters, see Table 1, and represents an improvement of the EXAFS study of Prestipino *et al.*[36] The same structural model was adopted for the analysis of the dehydrated sample, before and after interaction with ammonia. In the former case, the paths involving the water molecule (O_{H2O}) were excluded (resulting in 12 independent parameters); whereas in the latter no changes were done, since O atom (of H_2O) and N atom (of NH_3) are not distinguishable by EXAFS. In that case, the amplitude factor S_0^2 was fixed to the value obtained for the as-prepared sample (resulting in 13 independent parameters).

Figure 3b – d show the experimental signals for the three investigated samples and the different paths contribution to the Imm(FT), whereas Table 1 summarizes the optimized parameters. In all the three cases, the simulated EXAFS spectra well reproduce the experimental curves, as proved by the R-factor values that are always lower than 5%. In many cases, different scattering paths contributing in the same distance range are characterized by Imm(FT) in anti-phase; their contributions to the overall signal is consequently cancelled, because of destructive interference. This is particular evident in the first shell region for the dehydrated sample in interaction with NH_3 (Figure 3d), where the SS N_{NH3} path is in partial anti-phase with the SS C contribution, and the MS C–O1 and SS O2 contributions are characterized by a partial mutual depletion, globally resulting in a drastic erosion of the EXAFS signal. Although rare, such "cancellation" effect has already been observed in EXAFS studies on other materials: particularly relevant is the strong amplitude reduction of the second shell peak in Ga K–edge EXAFS spectra of $In_xGa_{1-x}As$ semiconductor solid solutions when x is close to 0.5.[76,85,86]
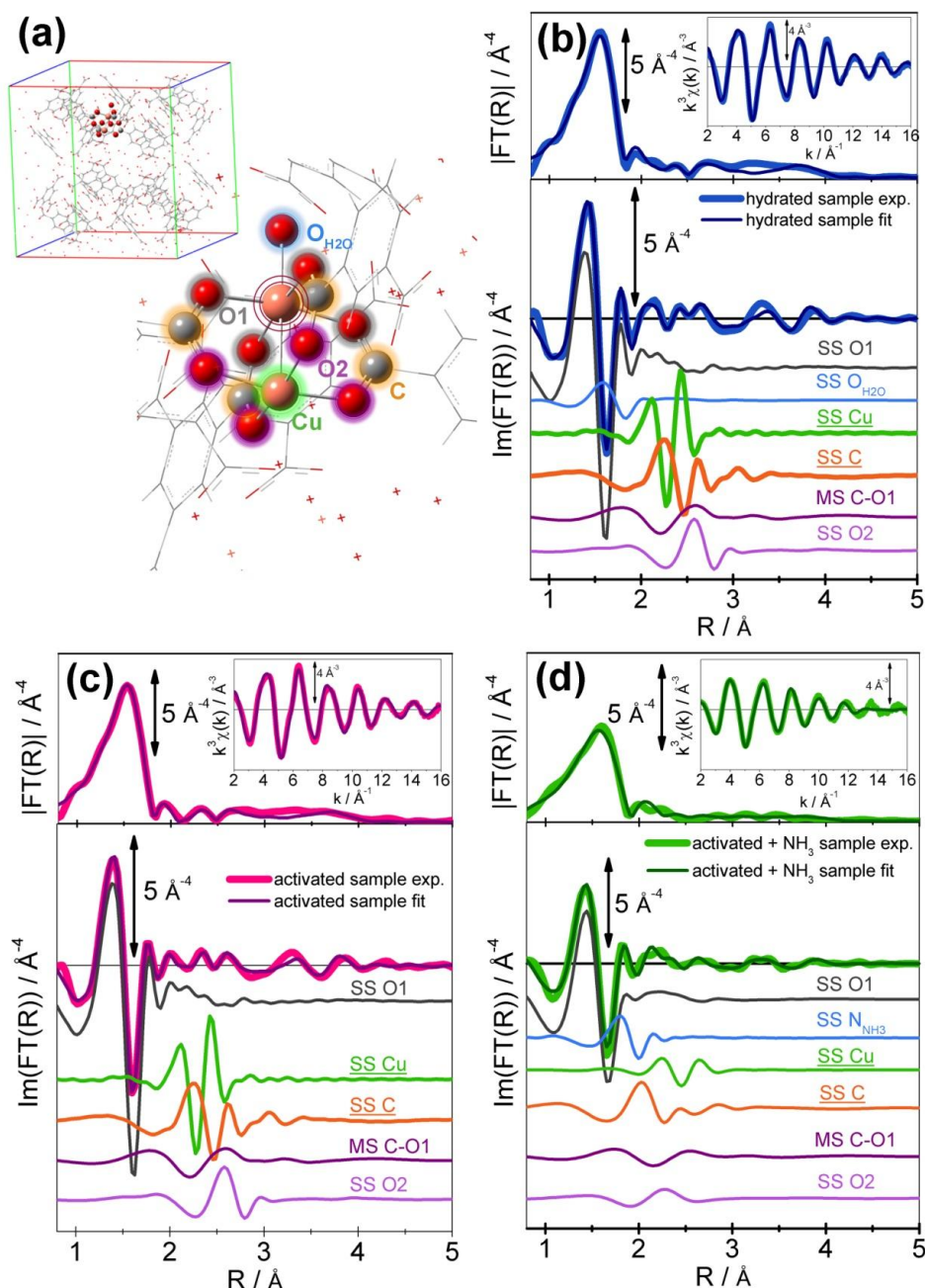
Figure 3. Part (a): Structure of the as-such sample obtained from a previous XRD refinement, and magnification of the cluster used as starting point for the fitting procedure of EXAFS data. Atoms color code is the following: Cu pale pink, C gray, O red. The groups of atoms involved in the principal paths contributing to EXAFS signal are labeled and highlighted by different colored halos (oxygen atoms of the trimesic acid carboxyl groups directly coordinated to the Cu_{abs}, O1, gray; oxygen of the water molecule directly coordinated to the Cu absorber, O_{H2O}, light blue; second copper atom of the dimer in front of the absorber, Cu, green; the four carbon atoms of the trimesic acid carboxyl groups, C, orange; oxygen atoms coordinated to the not absorber copper site, O2, purple). Parts (b), (c) and (d): Comparison between experimental and corresponding best fits for the as-such (b), activated (c) and activated + NH_3 (d) sample. Top panels report the modulus of the FT, while bottom panels show the imaginary parts of the FT, and the principal paths contributions to the total signal. For quantitative values of the parameters optimized in the fits, see Table 1.

Table 1. Summary of the parameters optimized in the fit of the EXAFS data (Figure 3b – d) for HKUST-1 samples as such, dehydrated and after exposure to 60 mbar of NH_3. All the fits were performed in R-space in the $\Delta R = 1.00 - 5.00$ Å range, over k^3-weighted FT of the $\chi(k)$ functions

performed in the 2 – 16 $Å^{-1}$ interval. A single ΔE_0 and a single S_0^2 have been employed to parametrize all SS and MS paths. In the activated + NH_3 case the amplitude S_0^2 was fixed to the value refined for hydrated sample ($S_0^2 = 0.99 \pm 0.05$), where the Cu centre is expected to have the same coordination number. For all paths the degeneration (coordination number for SS paths) has been fixed to the values expected from the structure refined by single crystal XRD.[32]

EXAFS optimized parameters			
	As such (hydrated)	Activated (dehydrated)	Activated + NH_3
Independent points	35	35	35
Number of variables	14	12	13
R-factor	0.014	0.010	0.018
S_0^2	0.99 ± 0.05	0.81 ± 0.03	0.99 ± 0.05
ΔE (eV)	-2.7 ± 0.6	-3.6 ± 0.5	-3.1 ± 0.5
R_{O1} (Å)	1.959 ± 0.005	1.934 ± 0.005	2.000 ± 0.004
σ^2_{O1} (Å^2)	0.0054 ± 0.0007	0.0051 ± 0.0006	0.0094 ± 0.0003
$R_{O(H2O)}$ or $R_{N(NH3)}$ (Å)	2.24 ± 0.03	–	2.31 ± 0.01
$\sigma^2_{O(H2O)}$ or $\sigma^2_{N(NH3)}$ (Å^2)	0.011 ± 0.006	–	0.006 ± 0.002
R_{Cu} (Å)	2.65 ± 0.02	2.58 ± 0.02	2.80 ± 0.03
σ^2_{Cu} (Å^2)	0.012 ± 0.002	0.015 ± 0.003	0.013 ± 0.03
R_C (Å)	2.88 ± 0.02	2.84 ± 0.02	2.56 ± 0.03
σ^2_C (Å^2)	0.008 ± 0.002	0.008 ± 0.001	0.013 ± 0.005
R_{O2} (Å)	3.14 ± 0.03	3.07 ± 0.03	2.82 ± 0.04
σ^2_{O2} (Å^2)	0.021 ± 0.005	0.024 ± 0.005	0.03 ± 0.01
α	-0.012 ± 0.004	-0.021 ± 0.004	-0.003 ± 0.002
σ^2 (Å^2)	0.009 ± 0.002	0.009 ± 0.002	0.016 ± 0.002

In the reported fits all coordination numbers were fixed to the crystallographic values. This holds also for the number of water (column 2) and ammonia (column 4) adsorbed on Cu(II) site (N_{ads}), that was fixed to unit in both cases. To check the adsorption stoichiometry additional fits were performed optimizing also the number of adsorbed molecules: N_{ads} resulted to be 1.04 ± 0.08 and 1.0 ± 0.1 for H_2O and NH_3, respectively.

The optimized parameters resulting from the fit are summarized in Table 1. For the as prepared sample, almost all the optimized distances are within their associated error equal to the ones extracted from single crystal XRD data of Chui *et al.*[32] or slightly longer. Upon activation, a generalized contraction of the bond lengths is observed, as already reported by Prestipino et al.[36] This contraction, particularly evident for the Cu_{abs}–Cu distance, is also observed by a negative value of the contraction/expansion parameter $\alpha = -0.021 \pm 0.004$. The Debye-Waller factors assume physically plausible values for all the different shells of atoms. Only the value for the oxygen atoms

coordinated to the not-absorber copper site (O2) is high because of a high static disorder term, due to the higher heterogeneity of the corresponding sites, not directly bonded to Cu_{abs}.

When the dehydrated sample is treated with ammonia, an increase in the Cu_{abs}–O1 average bond distance is observed (R_{O1} = 2.000 ± 0.004 Å), accompanied by an increase in the Debye-Waller factor σ^2_{O1}, which goes from ca. 0.005 Å^2 to 0.009 Å^2. The optimized Cu_{abs}–N_{NH3} bond distance value obtained from the fit is of (2.31 ± 0.01) Å, with a Debye Waller value $\sigma^2_{N(NH3)}$ = (0.006 ± 0.002) Å^2. Therefore, EXAFS data provide an evidence that adsorption of ammonia on the coordinative vacancy of Cu(II) in dehydrated HKUST-1 occurs without the break of any first shell Cu–O1 bonds, that just undergo an elongation of ~ 0.050 Å to accommodate the NH_3 molecule. This elongation is more than double than that needed to accommodate the water molecule, see Table 1. Additional structural distortions involve the higher shells, in particular (i) the Cu_{abs}–Cu bond is elongated of ~ 0.15 Å; and (ii) the Cu–C and Cu–O2 bond lengths are slightly contracted. Finally, it is worth noticing that fit results are affected by a higher degree of incertitude with respect to the as-such and activated cases, due to the lower signal-to-noise ratio and the possibility of different structural rearrangements resulting in the same signal suppression. A general increase of the DW values associated to C and O2 shells, as well as of the σ^2 Debye-Waller used to model SS and MS paths whose contribution to EXAFS signal is minor, is found.

3.3. Optical properties: DRUV-Vis spectroscopy

Upon activation the color of HKUST-1 changes from light cyan (Figure 4a) to blue navy (Figure 4b, first tube). To explain this behavior a change in the coordination sphere of copper species should be invoked, as the color is associated with d-d transitions of Cu(II) ions. The DRUV-Vis spectra of the as synthesized and activated samples are reported in Figure 4c (blue and pink lines, respectively). The spectrum of the fresh sample (blue curve) shows: i) an edge around 350 nm due to a ligand to metal charge transfer (LMCT) transition from oxygen to copper atoms; and ii) a band centered at about 705 nm, characteristic of d-d transition for Cu(II) species in a distorted octahedral local geometry. The distorsion of the octahedral geometry accounts for the high intensity of the band, that should be otherwise dipole-forbidden.

The main effect of activation at 423 K (pink curve) is the appearance of a high-energy shoulder in the d-d band at around 585 nm. At the same time, a red shift of the maximum, previously observed at 705 nm, to 745 nm and of the absorption associated with the LMCT transition are observed. The increase of the fraction of absorbed visible light causes a complete darkening of the material, which changes from light cyan to blue navy. The change in the d-d region is ascribed to the activation of new available d-d transitions due to a loss of degeneracy in d levels produced by a change in the symmetry around copper. Coming to the high-energy part of the UV-Vis spectrum, the LMCT edge shift is explained as a consequence of the change of (i) the hydration conditions of the carboxylated group and (ii) the coordination sphere of copper ions. [36] Upon H_2O vapor pressure dosage on the activated sample, the original spectrum is restored (orange solid curve), demonstrating the reversibility of the process. [36] If pure dry ammonia is dosed on the activated material, the spectrum (green solid curve) is quite similar to that of the hydrated sample, apart for a slight red shift of the d-d band to 725 nm. This small shift is sufficient to cause a color change, as demonstrated by the sequence of photographs reported in Figure 4b, collected at increasing NH_3 contact time.
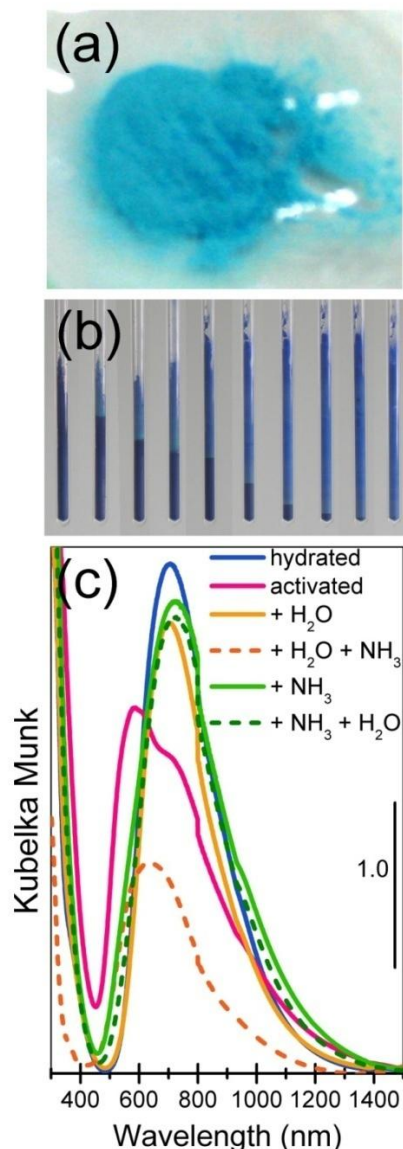
Figure 4. Part (a): picture of hydrated HKUST-1 sample. Part (b): sequence of pictures showing the HKUST-1 color evolution upon NH_3 dosage and progressive advance of the NH_3 front, starting from the activated material (first tube). Part (c): DRUV-Vis spectra of HKUST-1 as prepared (blue line), activated (pink line), activated + H_2O and successively + NH_3 (orange solid and dashed line respectively), activated + NH_3 and successively + H_2O (green solid and dashed line respectively).

On the contrary, the dosage of ammonia on a sample previously contacted with water vapor pressure causes a big change in the spectrum (see orange dashed line), providing an evidence that the coordination sphere of Cu(II) is strongly perturbed. The effect of water after pure ammonia adsorption has been considered too and the resulting spectrum is almost unperturbed (see green dashed curve). These results are in good agreement with the XRPD ones.

3.4. Vibrational properties: IR spectroscopy

The vibrational properties of HKUST-1 in the Mid-IR range have been studied by collecting the spectra in ATR mode (see Figure 5a). In this frequency range, the spectra of hydrated sample HKUST-1 is dominated by the vibrational modes of the BTC linker. In particular, the IR absorption bands in the 1700-1500 cm^{-1} and 1500-1300 cm^{-1} range are due to $\upsilon_{asym}(C-O_2)$ and $\upsilon_{sym}(C-O_2)$ stretching mode, respectively; IR bands around 1450 cm^{-1} are due to a combination of benzene ring stretching and deformation modes; whereas, IR absorption bands around 700 cm^{-1} are due to υ (C−

13

H) bending mode. Only the IR absorption band centered at 493 cm^{-1} is due to a vibrational mode directly involving the Cu center, and it will be discussed later on.

The Mid-IR spectrum of HKUST-1 does not change upon dehydration (only the broad IR absorption band centered at 3300 cm^{-1} disappears), neither upon adsorption of NH$_3$ (apart a slight broadening of most of the IR absorption bands). On the contrary, the spectrum greatly changed when ammonia is dosed on the hydrated sample. In particular, in the 1700 – 1500 cm^{-1} range only two distinct absorption bands are observed at 1610 and 1544 cm^{-1}; the IR bands in the 1500 – 1300 cm^{-1} are slightly red shifted; new IR absorption bands appear at 1250, 1213 and 708 cm^{-1}. Although further investigation is necessary to assign precisely the new IR absorption bands, the Mid-IR spectrum of the hydrated sample after interaction with ammonia is clearly in favor of a big structural change, in agreement with all the data discussed above.
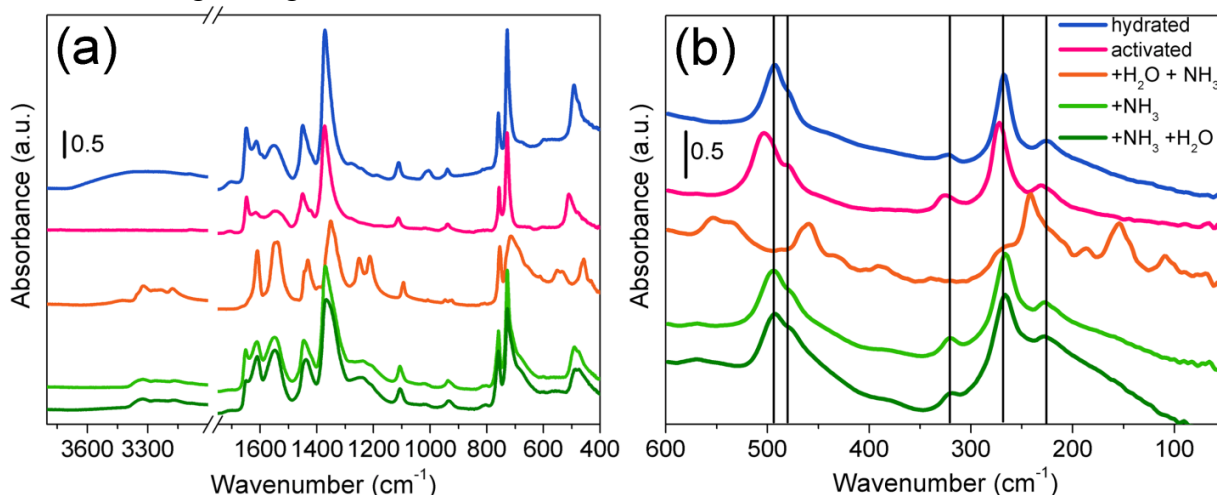

Figure 5. Mid-IR (ATR mode), part (a), and Far-IR (transmittance mode), part (b), spectra of HKUST-1 as prepared (blue line), activated (pink line), activated + H$_2$O and + NH$_3$ (orange line), activated + NH$_3$ (light green line) and successively + H$_2$O (dark green line).

IR spectra in the Far-IR region (see Figure 5b), are much more informative, since in the 600 – 50 cm^{-1} range the vibrational modes directly involving Cu(II) species are present. The same frequencies range was previously explored in detail by means of Raman spectroscopy [36] for the hydrated and activated sample. The Far-IR spectrum of the hydrated sample (blue curve) shows two main absorption regions, around 500 cm^{-1} (main peak at 493 cm^{-1} and shoulder at 480 cm^{-1}) and around 280 cm^{-1} (three absorption bands centered at 321, 269 (the most intense) and 226 cm^{-1}). Following the previous interpretation,[36] the IR absorption bands around 500 cm^{-1} are assigned to Cu – O stretching modes , while the absorption bands at lower frequency are due to vibrational modes involving the Cu – Cu stretching of the two Cu(II) ions of the [Cu$_2$C$_4$O$_8$] framework cage. Upon activation, both the IR absorption band at 493 cm^{-1} and the three bands at lower frequency blue-shift; to 504 cm^{-1}, 326, 273 and 231 cm^{-1}, respectively. This observation reveals an increase in rigidity of the metallorganic framework structure, in agreement with the shortening of the Cu-O and Cu-Cu bonds obtained by EXAFS. Finally, when ammonia is adsorbed on the dehydrated sample (light green spectrum) the Far-IR spectrum comes back to that of the hydrated sample; whereas interaction of ammonia on a hydrated sample causes a drastic change of the overall spectrum.

3.5. EPR characterization

The CW-EPR spectrum of hydrated HKUST-1 is characterized by a typical anisotropic powder pattern characteristic of hydrated Cu(II) ions having an electron spin $S = 1/2$ and interacting with the $I = 3/2$ nuclear spin of the copper nuclei (Figure 6A, blue line). The parameters derived from the simulation (Figure 6A, dotted line) are listed in Table 2 and are in agreement with those previously reported by Pöppl et al.[87-90] on the same system.
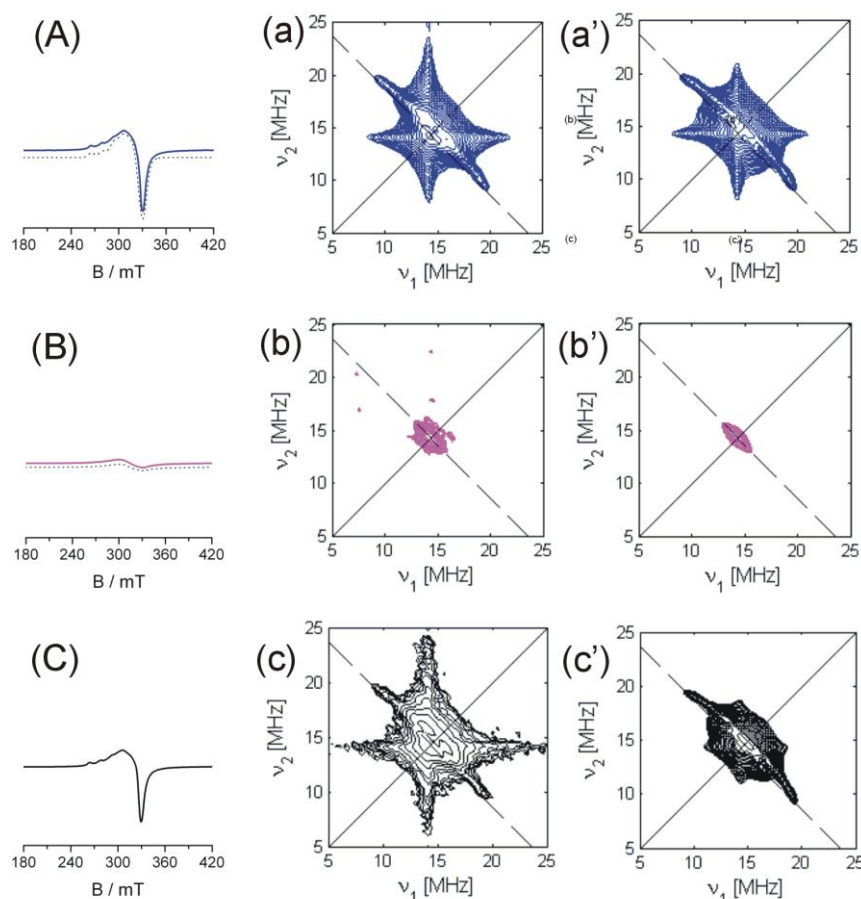
Figure 6. Parts (A), (B), (C): experimental (solid lines) and simulated (dotted lines) X-band CW-EPR spectra of hydrated (blue line), dehydrated (pink line) and re-hydrated (black line) HKUST-1; parts (a), (b) and (c): experimental ^{1}H HYSCORE spectra; parts (a'), (b') and (c') are the corresponding computer simulations. All spectra were recorded at 10K. The HYSCORE spectra were taken at observer position B_0= 336 mT, corresponding to the $g_\perp$ component of the field swept spectrum. Two spectra measured with τ = 104 and 172 ns are added together after Fourier transform.

The spectrum consists of two superimposed signals, indicated in Table 1 as type A Cu(II) and type B Cu(II). The spin Hamiltonian parameters of type A are typical for isolated Cu(II) hydrated monomers, while the second species (type B), characterized by a broad unresolved line, with ΔB^{PP} = 30 mT and g_{av}=2.17 has been assigned to interacting Cu(II) species.[87]

Quantitative evaluation of the monomeric copper species in the hydrated sample has been obtained by comparison of the CW EPR spectral intensity with that of a standard solution of copper acetylacetonate. The estimated percentage of isolated Cu(II) ions is found to be about 6% of the overall copper ions in the sample. In agreement with earlier literature reports, [87] we assign such isolated (S=1/2) Cu(II) species to residual extra-framework monomeric Cu(II) ions, which have not been incorporated as [Cu(II)]$_2$ dimers in the Cu$_3$(BTC)$_2$ network.

Upon dehydration at 423K under vacuum the sample develops a blue navy colour and shows the EPR spectrum of Figure 6B (pink line). The signal due to the monomeric Cu(II) ions is drastically reduced in intensity, while the broad signal due to interacting copper species (type B) becomes evident. The overall decrease of the EPR spectral intensity is about 20% of the hydrated spectrum (blue line). The original spectrum can be restored by hydration of the sample (Figure 6C, black line).

Table 2. Spin Hamiltonian parameters of Cu(II) species in HKUST-1 obtained by computer simulation of the spectra in Figure 6.

Cu(II) spin Hamiltonian parameters from X-band CW-EPR spectra

	g tensor	Hyperfine tensor ^{Cu}A/MHz
Type A Cu(II)	$g_\parallel = 2.374 \pm 0.001$	$A_\parallel = 456 \pm 3$
	$g_\perp = 2.089 \pm 0.007$	$A_\perp = 73 \pm 12$
Type B Cu(II)	$g = 2.17 \pm 0.02$	-

To investigate more deeply the effects caused by dehydration and rehydration of the sample and in the effort of better characterizing the local coordination environment of the Cu(II) monomers, Hyperfine Sublevel Correlation (HYSCORE) measurements were carried out.

The HYSCORE spectra recorded at observer position $B_0 = 336$ mT, corresponding to the Cu(II) perpendicular feature, are reported in Figure 6a, b and c (spectra taken at a magnetic field setting corresponding to the parallel position are reported as supplementary information). The spectrum of the hydrated material (Figure 6a) is characterized by a pronounced broad proton ridge centred at (ν_H, ν_H) with maximum extension of about 11.8 MHz, stemming from the superhyperfine interaction between the unpaired electron in the d_{x2-y2} Cu(II) orbital and a nearby proton. The experimental spectrum can be simulated (Figure 6a') using the parameters reported in Table 3. These values are typical for water molecules equatorially coordinated to the Cu(II) ions,[91] and are in line with those found for the $Cu(H_2O)_6^{2+}$ complex.[92]

The simulation analysis indicates that the experimental spectrum is best reproduced by considering a second interacting proton with maximum coupling of about 3 MHz due to remote protons, weakly interacting with Cu(II) monomers.

Table 3. Spin Hamiltonian parameters deduced from simulation of the HYSCORE spectra of Figure 6a, d, and c.

Spin Hamiltonian parameters from simulation of the HYSCORE spectrum

Proton Species Interacting with Cu(II)	$^H a_{iso}$ /MHz	$^H T$ /MHz	$\alpha ; \beta ; \gamma$/°
A	0.2 ± 0.5	5.8 ± 0.5	$0 ; 70 \pm 10 ; 0$
B	0.4 ± 0.5	1.4 ± 0.5	$0 ; 60 \pm 10 ; 0$

The HYSCORE spectrum of the dehydrated sample, recorded at the same observer position is reported in Figure 6b. As a consequence of the dehydration treatment, the pronounced ridge with maximum coupling 11.8 MHz disappears, and only the small proton ridge with maximum extension of about 3 MHz is observed. Admission of water onto the dehydrated sample restores the original proton ridge (Figure 6c). This is in agreement with the CW-EPR spectrum reported in Figure 6C.

The hydration-dehydration behaviour of momomeric Cu(II) species in H-KUST is reminiscent of that of hydrated cupric Cu(II) ions in zeolites where the same phenomenon, *i.e.* an intensity drop of Cu(II) EPR spectra upon thermal treatment in vacuo and subsequent restoring by simple water adsorption at room temperature is well known.[64] This effect, often called "self-reduction" process, has been interpreted in the case of zeolites in term of a proper reduction mechanism involving the formation via different pathways of cuprous (diamagnetic) ions (Cu^+).[93,94] This interpretation was however challenged by LoJacono, and co-workers,[95] who suggested that the loss of intensity of the

EPR signal has to be ascribed to changes in the coordination of Cu(II) ions which become EPR inactive, without invoking the formation of Cu^+ ions. This second mechanism was later verified by a multytechnique approach.[64] Our experiments indeed show that this second mechanism is appropriate to describe the behavior of isolated Cu(II) ions in $Cu_3(btc)_2$. The phenomenon can in fact be explained considering that upon water removal at low temperature, the solvated Cu(II) ions undergo a local symmetry change, which is the ultimately responsible for the loss in the EPR signal. Re-hydration of the system will restore the original solvation shell thus explaining the recovery of the EPR signal and the easy reversibility of the process.
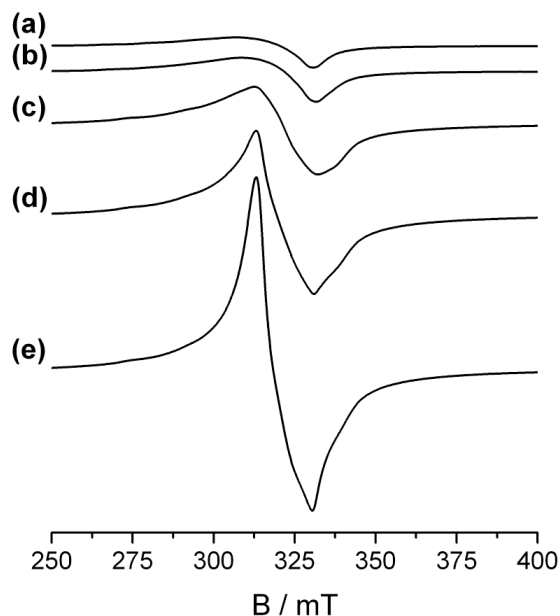

Figure 7. X-band CW EPR spectra of HKUST upon delivery of increasing amounts of ammonia. (a) hydrated sample, (b) 5 mbar NH_3, (c) 30 mbar NH_3,(d) 45 mbar NH_3 (e) 60 mbar NH_3. Spectra are recorded at 77K.

Following the procedure adopted for all the experiments we contacted the hydrated sample with increasing doses of ammonia at ambient temperature. This led to a progressive change of the CW EPR spectrum, up to the formation of a new, intense signal, characterized by an asymmetric line shape resonating at $g \approx 2.12$ whose intensity is about two orders of magnitude more intense with respect to the signal of the hydrated sample (Figure 6A). Figure 7 shows the evolution of the CW EPR spectrum as a function of ammonia dosage. The new signal starts to appear upon delivery of 30 mbar of NH_3 and shows no trace of the EPR features of isolated Cu(II) and no echo signals could be detected. Comparison of spectra taken in the range 300-6 K for an ammonia dosage of 30 mbar (Figure 8) shows that no significant modification in the spectral line shape occur in this temperature range. The signal intensity, however, increases with lowering temperature following a Curie like behavior (see inset Figure 8), typical of a paramagnetic state. The loss of Cu(II) hyperfine structure seems to indicate that spin exchange phenomena are under operation which involve a large fraction of the copper ions including framework ions. These phenomena will lead to an increase in the relaxation times of the system explaining the absence of the spin echo signal. The same behavior described above, at least qualitatively, was observed in case of NH_3 dosage in dry conditions.
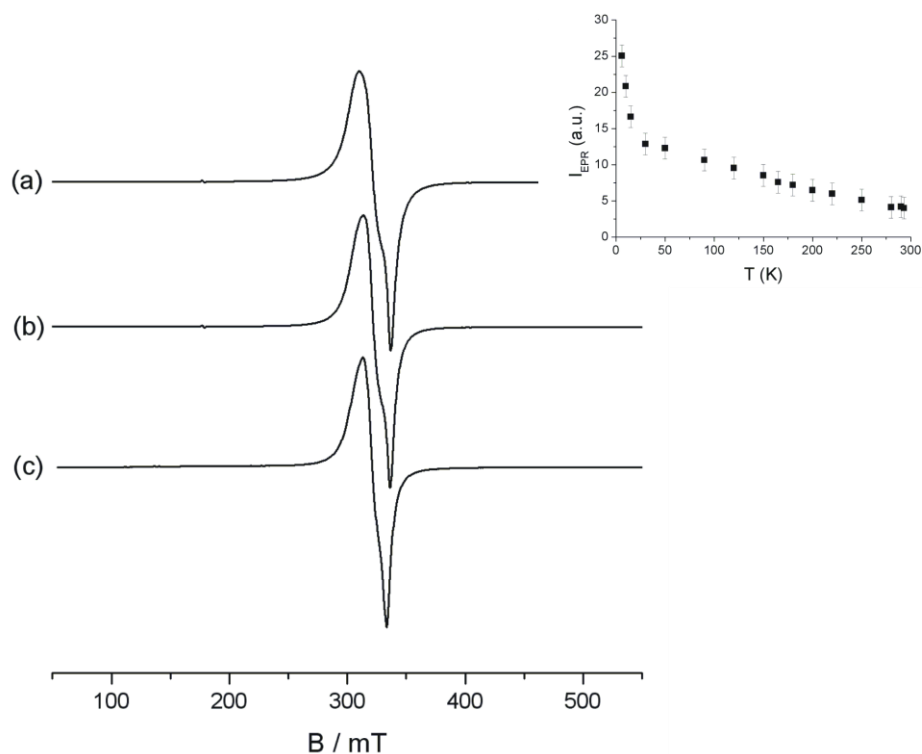
Figure 8. CW EPR spectra of HKUST-1 upon delivery of 30 mbar of NH_3 recorded at (a) 6 K, (b) 90 K and (c) 300 K. The scattered plot in the inset reports the EPR intensity of the spectra recorded at temperatures ranging from 6 to 300 K.

Outgassing of the cell did not restore the original EPR spectrum indicating that the effect, contrary to water adsorption is not reversible and that interaction with NH_3 leads to a stable modification of the magnetic properties of the sample. Further investigations will be needed to specifically address the nature of the magnetic properties brought about by ammonia adsorption.

4. Conclusions

A full spectroscopic characterization of HKUST-1 interacting with ammonia has been presented. NH_3 adsorption on the dry system results in a strong chemisorption on Cu(II) sites that distorts the framework, keeping the crystallinity of the material. Generally the perturbation observed upon NH_3 adsorption is analogue to the one observed in the case of H_2O, but noticeably enhanced. When the adsorption in humid conditions is considered, a deep modification of the system is observed. In particular, i) XRPD shows a very strong interaction in dry conditions and strong modification of the structure in presence of water; ii) XAS (XANES and EXAFS) spectroscopy, in dry conditions, indicates structural changes, similar to the case of H_2O but quantitatively bigger; iii) both DRUV-Visible and IR (MIR and Far-IR frequencies range) spectroscopies indicate a similarity between the hydrated sample and the one interacting with NH_3 in dry conditions, but they reveal deep changes if NH_3 is adsorbed in humid conditions; iv) EPR technique reveals that the interaction with NH_3 both in dry and humid conditions leads to a stable modification of the magnetic properties of the sample.

On a methodological ground, it is worth noticing that we used the optimization of XANES spectra to validate the bond distance obtained by EXAFS.

In conclusion, this work demonstrates that to have a very deep structural modification of HKUST when NH_3 interaction is considered (as e.g. reported in literature by Peterson et al.[39]), the water presence is necessary, otherwise the modification occurs but with minor effect.

Corresponding Author

*Francesca Bonino : francesca.bonino@unito.it

Author Contributions

The manuscript was written through contributions of all authors. All authors have given approval to the final version of the manuscript.

Supporting Information

Experimental and simulated HYSCORE spectra at $g_{\parallel}$ position.

TOC
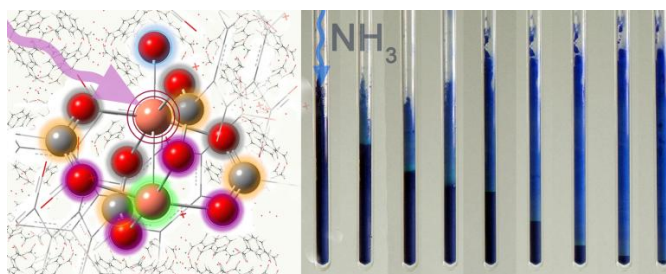
References and Notes

(1) Cheetham, A. K.; Ferey, G.; Loiseau, T. *Angew. Chem.-Int. Edit.* **1999**, *38*, 3268-3292.

(2) James, S. L. *Chem. Soc. Rev.* **2003**, *32*, 276-288.

(3) Kitagawa, S.; Kitaura, R.; Noro, S. *Angew. Chem.-Int. Edit.* **2004**, *43*, 2334-2375.

(4) Bradshaw, D.; Claridge, J. B.; Cussen, E. J.; Prior, T. J.; Rosseinsky, M. J. *Acc. Chem. Res.* **2005**, *38*, 273-282.

(5) Ferey, G. *Chem. Soc. Rev.* **2008**, *37*, 191-214.

(6) Farha, O. K.; Hupp, J. T. *Acc. Chem. Res.* **2010**, *43*, 1166-1175.

(7) Stock, N.; Biswas, S. *Chem. Rev.* **2012**, *112*, 933-969.

(8) Meek, S. T.; Greathouse, J. A.; Allendorf, M. D. *Adv. Mater.* **2011**, *23*, 249-267.

(9) Wu, C. D.; Hu, A.; Zhang, L.; Lin, W. B. *J. Am. Chem. Soc.* **2005**, *127*, 8940-8941.

(10) Dybtsev, D. N.; Nuzhdin, A. L.; Chun, H.; Bryliakov, K. P.; Talsi, E. P.; Fedin, V. P.; Kim, K., A *Angew. Chem.-Int. Edit.* **2006**, *45*, 916-920.

(11) Llabrés i Xamena, F. X.; Abad, A.; Corma, A.; Garcia, H. *J. Catal.* **2007**, *250*, 294-298.

(12) Horike, S.; Dinca, M.; Tamaki, K.; Long, J. R. *J. Am. Chem. Soc* **2008**, *130*, 5854-5855.

(13) Savonnet, M.; Aguado, S.; Ravon, U.; Bazer-Bachi, D.; Lecocq, V.; Bats, N.; Pinel, C.; Farrusseng, D. *Green Chem.* **2009**, *11*, 1729-1732.

(14) Lee, J.; Farha, O. K.; Roberts, J.; Scheidt, K. A.; Nguyen, S. T.; Hupp, J. T. *Chem. Soc. Rev.* **2009**, *38*, 1450-1459.

(15) Shultz, A. M.; Farha, O. K.; Hupp, J. T.; Nguyen, S. T. *J. Am. Chem. Soc.* **2009**, *131*, 4204-4205.

(16) Ma, L.; Abney, C.; Lin, W. *Chem. Soc. Rev.* **2009**, *38*, 1248-1256.

(17) Corma, A.; Garcıa, H.; Llabres i Xamena, F. X. *Chem. Rev.* **2010**, *110*, 4606-4655.

(18) Luz, I.; Xamena, F.; Corma, A. *J. Catal.* **2012**, *285*, 285-291.

(19) Aguado, S.; Canivet, J.; Schuurman, Y.; Farrusseng, D. *J. Catal.* **2011**, *284*, 207-214.

(20) Eddaoudi, M.; Kim, J.; Rosi, N.; Vodak, D.; Wachter, J.; O'Keeffe, M.; Yaghi, O. M. *Science* **2002**, *295*, 469-472.

(21) Dinca, M.; Long, J. R. *J. Am. Chem. Soc.* **2005**, *127*, 9376-9377.

(22) Dinca, M.; Dailly, A.; Liu, Y.; Brown, C. M.; Neumann, D. A.; Long, J. R. *J. Am. Chem. Soc.* **2006**, *128*, 16876-16883.

(23) Vitillo, J. G.; Regli, L.; Chavan, S.; Ricchiardi, G.; Spoto, G.; Dietzel, P. D. C.; Bordiga, S.; Zecchina, A. *J. Am. Chem. Soc.* **2008**, *130*, 8386-8396.

(24) Dietzel, P. D. C.; Johnsen, R. E.; Fjellvag, H.; Bordiga, S.; Groppo, E.; Chavan, S.; Blom, R. *Chem. Commun.* **2008**, 5125-5127.

(25) Murray, L. J.; Dinca, M.; Long, J. R. *Chem. Soc. Rev.* **2009**, *38*, 1294-1314.

(26) Li, J.-R.; Luppler, R. J.; Zhou, H. C. *Chem. Soc. Rev.* **2009**, *38*, 1477-1504.

(27) Britt, D.; Furukawa, H.; Wang, B.; Glover, T. G.; Yaghi, O. M. *Proc. Natl. Acad. Sci. USA* **2009**, *106*, 20637-20640.

(28) Sato, H.; Matsuda, R.; Sugimoto, K.; Takata, M.; Kitagawa, S. *Nat. Mater.* **2010**, *9*, 661-666.

(29) Shimomura, S.; Higuchi, M.; Matsuda, R.; Yoneda, K.; Hijikata, Y.; Kubota, Y.; Mita, Y.; Kim, J.; Takata, M.; Kitagawa, S. *Nat. Chem.* **2010**, *2*, 633-637.

(30) Hamon, L.; Heymans, N.; Llewellyn, P. L.; Guillerm, V.; Ghoufi, A.; Vaesen, S.; Maurin, G.; Serre, C.; De Weireld, G.; Pirngruber, G. D. *Dalton Trans.* **2012**, *41*, 4052-4059.

(31) Chavan, S.; Vitillo, J. G.; Gianolio, D.; Zavorotynska, O.; Civalleri, B.; Jakobsen, S.; Nilsen, M. H.; Valenzano, L.; Lamberti, C.; Lillerud, K. P. et al. *Phys. Chem. Chem. Phys.* **2012**, *14*, 1614-1626.

(32) Chui, S. S. Y.; Lo, S. M. F.; Charmant, J. P. H.; Orpen, A. G.; Williams, I. D. *Science* **1999**, *283*, 1148-1150.

(33) Wang, Q. M.; Shen, D. M.; Bulow, M.; Lau, M. L.; Deng, S. G.; Fitch, F. R.; Lemcoff, N. O.; Semanscin, J. *Microporous Mesoporous Mater.* **2002**, *55*, 217-230.

(34) Xiao, B.; Wheatley, P. S.; Zhao, X. B.; Fletcher, A. J.; Fox, S.; Rossi, A. G.; Megson, I. L.; Bordiga, S.; Regli, L.; Thomas, K. M. et al. *J. Am. Chem. Soc.* **2007**, *129*, 1203-1209.

(35) Bordiga, S.; Regli, L.; Bonino, F.; Groppo, E.; Lamberti, C.; Xiao, B.; Wheatley, P. S.; Morris, R. E.; Zecchina, A. *Phys. Chem. Chem. Phys.* **2007**, *9*, 2676-2685.

(36) Prestipino, C.; Regli, L.; Vitillo, J. G.; Bonino, F.; Damin, A.; Lamberti, C.; Zecchina, A.; Solari, P. L.; Kongshaug, K. O.; Bordiga, S. *Chem. Mater.* **2006**, *18*, 1337-1346.

(37) Zhang, X. X.; Chui, S. S. Y.; Williams, I. D. *J. Appl. Phys.* **2000**, *87*, 6007-6009.

(38) Schlichte, K.; Kratzke, T.; Kaskel, S. *Microporous Mesoporous Mater.* **2004**, *73*, 81-88.

(39) Peterson, G. W.; Wagner, G. W.; Balboa, A.; Mahle, J.; Sewell, T.; Karwacki, C. J. *J. Phys. Chem. C* **2009**, *113*, 13906-13917.

(40) Petit, C.; Bandosz, T. J. *Dalton Trans.* **2012**, *41*, 4027-4035.

(41) Petit, C.; Huang, L. L.; Jagiello, J.; Kenvin, J.; Gubbins, K. E.; Bandosz, T. J. *Langmuir* **2011**, *27*, 13043-13051.

(42) Petit, C.; Mendoza, B.; Bandosz, T. J. *Langmuir* **2010**, *26*, 15302-15309.

(43) Saha, D. P.; Deng, S. G. *J. Colloid Interface Sci.* **2010**, *348*, 615-620.

(44) Guo, X. J.; Tak, J. K.; Johnson, R. L. *J. Hazard. Mater.* **2009**, *166*, 372-376.

(45) Arreola, R.; Valderrama, B.; Morante, M. L.; Horjales, E. *FEBS Lett.* **2003**, *551*, 63-70.

(46) Britt, D.; Tranchemontagne, D.; Yaghi, O. M. *Proc. Natl. Acad. Sci. USA* **2008**, *105*, 11623-11627.

(47) Kusgens, P.; Rose, M.; Senkovska, I.; Frode, H.; Henschel, A.; Siegle, S.; Kaskel, S. *Microporous Mesoporous Mater.* **2009**, *120*, 325-330.

(48) Nikitenko, S.; Beale, A. M.; van der Eerden, A. M. J.; Jacques, S. D. M.; Leynaud, O.; O'Brien, M. G.; Detollenaere, D.; Kaptein, R.; Weckhuysen, B. M.; Bras, W. *J. Synchrot. Radiat.* **2008**, *15*, 632-640.

(49) Silversmit, G.; Vekemans, B.; Nikitenko, S.; Bras, W.; Czhech, V.; Zaray, G.; Szaloki, I.; Vincze, L. *J. Synchrot. Radiat.* **2009**, *16*, 237-246.

(50) Lamberti, C.; Prestipino, C.; Bordiga, S.; Berlier, G.; Spoto, G.; Zecchina, A.; Laloni, A.; La Manna, F.; D'Anca, F.; Felici, R. et al. *Nucl. Instrum. Methods Phys. Res. Sect. B-Beam Interact. Mater. Atoms* **2003**, *200*, 196-201.

(51) Lamberti, C.; Bordiga, S.; Bonino, F.; Prestipino, C.; Berlier, G.; Capello, L.; D'Acapito, F.; Xamena, F.; Zecchina, A. *Phys. Chem. Chem. Phys.* **2003**, *5*, 4502-4509.

(52) Ravel, B.; Newville, M. *J. Synchrot. Radiat.* **2005**, *12*, 537-541.

(53) Lamberti, C.; Bordiga, S.; Arduino, D.; Zecchina, A.; Geobaldo, F.; Spanò, G.; Genoni, F.; Petrini, G.; Carati, A.; Villain, F. et al. *J. Phys. Chem. B* **1998**, *102*, 6382-6390.

(54) Bordiga, S.; Bonino, F.; Lillerud, K. P.; Lamberti, C. *Chem. Soc. Rev.* **2010**, *39*, 4885-4927.

(55) Zabinsky, S. I.; Rehr, J. J.; Ankudinov, A.; Albers, R. C.; Eller, M. J. *Phys. Rev. B* **1995**, *52*, 2995-3009.

(56) Ankudinov, A. L.; Rehr, J. J. *Phys. Rev. B* **2000**, *62*, 2437-2445.

(57) Smolentsev, G.; Soldatov, A. *J. Synchrot. Radiat.* **2006**, *13*, 19-29.

(58) Spalek, T.; Pietrzyk, P.; Sojka, Z. *J. Chem Inf. Model.* **2005**, *45*, 18-29.

(59) Hofer, P.; Grupp, A.; Nebenfuhr, H.; Mehring, M. *Chem. Phys. Lett.* **1986**, *132*, 279-282.

(60) Stoll, S.; Schweiger, A. *J. Magn. Reson.* **2006**, *178*, 42-55.

(61) Lamberti, C.; Spoto, G.; Scarano, D.; Paze, C.; Salvalaggio, M.; Bordiga, S.; Zecchina, A.; Palomino, G. T.; Dacapito, F. *Chem. Phys. Lett.* **1997**, *269*, 500-508.

(62) Lamberti, C.; Bordiga, S.; Zecchina, A.; Salvalaggio, M.; Geobaldo, F.; Arean, C. O. *J. Chem. Soc.-Faraday Trans.* **1998**, *94*, 1519-1525.

(63) Bolis, V.; Maggiorini, S.; Meda, L.; D'Acapito, F.; Palomino, G. T.; Bordiga, S.; Lamberti, C. *J. Chem. Phys.* **2000**, *113*, 9248-9261.

(64) Turnes Palomino, G.; Fisicaro, P.; Bordiga, S.; Zecchina, A.; Giamello, E.; Lamberti, C. *J. Phys. Chem. B* **2000**, *104*, 4064-4073.

(65) Lamberti, C.; Prestipino, C.; Bonino, F.; Capello, L.; Bordiga, S.; Spoto, G.; Zecchina, A.; Moreno, S. D.; Cremaschi, B.; Garilli, M. et al. *Angew. Chem.-Int. Edit.* **2002**, *41*, 2341-2344.

(66) Prestipino, C.; Berlier, G.; Xamena, F.; Spoto, G.; Bordiga, S.; Zecchina, A.; Palomino, G. T.; Yamamoto, T.; Lamberti, C. *Chem. Phys. Lett.* **2002**, *363*, 389-396.

(67) Prestipino, C.; Bordiga, S.; Lamberti, C.; Vidotto, S.; Garilli, M.; Cremaschi, B.; Marsella, A.; Leofanti, G.; Fisicaro, P.; Spoto, G. et al. *J. Phys. Chem. B* **2003**, *107*, 5022-5030.

(68) Llabrés i Xamena , F. X.; Fisicaro, P.; Berlier, G.; Zecchina, A.; Palomino, G. T.; Prestipino, C.; Bordiga, S.; Giamello, E.; Lamberti, C. *J. Phys. Chem. B* **2003**, *107*, 7036-7044.

(69) Prestipino, C.; Capello, L.; D'Acapito, F.; Lamberti, C. *Phys. Chem. Chem. Phys.* **2005**, *7*, 1743-1746.

(70) Truccato, M.; Lamberti, C.; Prestipino, C.; Agostino, A. *Appl. Phys. Lett.* **2005**, *86*, art. n. 213116.

(71) Muddada, N. B.; Olsbye, U.; Caccialupi, L.; Cavani, F.; Leofanti, G.; Gianolio, D.; Bordiga, S.; Lamberti, C. *Phys. Chem. Chem. Phys.* **2010**, *12*, 5605-5618.

(72) Muddada, N. B.; Olsbye, U.; Leofanti, G.; Gianolio, D.; Bonino, F.; Bordiga, S.; Fuglerud, T.; Vidotto, S.; Marsella, A.; Lamberti, C. *Dalton Trans.* **2010**, *39*, 8437-8449.

(73) Groppo, E.; Prestipino, C.; Lamberti, C.; Luches, P.; Giovanardi, C.; Boscherini, F. *J. Phys. Chem. B* **2003**, *107*, 4597-4606.

(74) Lamberti, C.; Groppo, E.; Prestipino, C.; Casassa, S.; Ferrari, A. M.; Pisani, C.; Giovanardi, C.; Luches, P.; Valeri, S.; Boscherini, F. *Phys. Rev. Lett.* **2003**, *91*, art n. 046101.

(75) Groppo, E.; Prestipino, C.; Lamberti, C.; Carboni, R.; Boscherini, F.; Luches, P.; Valeri, S.; D'Addato, S. *Phys. Rev. B* **2004**, *70*, 165408.

(76) Lamberti, C. *Surf. Sci. Rep.* **2004**, *53*, 1-197.

(77) Piovano, A.; Agostini, G.; Frenkel, A. I.; Bertier, T.; Prestipino, C.; Ceretti, M.; Paulus, W.; Lamberti, C. *J. Phys. Chem. C* **2011**, *115*, 1311-1322.

(78) Cavka, J. H.; Jakobsen, S.; Olsbye, U.; Guillou, N.; Lamberti, C.; Bordiga, S.; Lillerud, K. P. *J. Am. Chem. Soc.* **2008**, *130*, 13850-13851.

(79) Bonino, F.; Chavan, S.; Vitillo, J. G.; Groppo, E.; Agostini, G.; Lamberti, C.; Dietzel, P. D. C.; Prestipino, C.; Bordiga, S. *Chem. Mater.* **2008**, *20*, 4957-4968.

(80) Chavan, S.; Bonino, F.; Vitillo, J. G.; Groppo, E.; Lamberti, C.; Dietzel, P. D. C.; Zecchina, A.; Bordiga, S. *Phys. Chem. Chem. Phys.* **2009**, *11*, 9811-9822.

(81) Masciocchi, N.; Galli, S.; Colombo, V.; Maspero, A.; Palmisano, G.; Seyyedi, B.; Lamberti, C.; Bordiga, S. *J. Am. Chem. Soc.* **2010**, *132*, 7902-7904.

(82) Valenzano, L.; Civalleri, B.; Bordiga, S.; Nilsen, M. H.; Jakobsen, S.; Lillerud, K.-P.; Lamberti, C. *Chem. Mater.* **2011**, *23*, 1700-1718.

(83) Valenzano, L.; Vitillo, J. G.; Chavan, S.; Civalleri, B.; Bonino, F.; Bordiga, S.; Lamberti, C. *Catal. Today* **2012**, *182*, 67-79.

(84) Rossin, A.; Di Credico, B.; Giambastiani, G.; Peruzzini, M.; Pescitelli, G.; Reginato, G.; Borfecchia, E.; Gianolio, D.; Lamberti, C.; Bordiga, S. *J. Mater. Chem.* **2012**, *22*, 10335-10344.

(85) Boscherini, F.; Lamberti, C.; Pascarelli, S.; Rigo, C.; Mobilio, S. *Phys. Rev. B* **1998**, *58*, 10745-10753.

(86) Romanato, F.; De Salvador, D.; Berti, M.; Drigo, A.; Natali, M.; Tormen, M.; Rossetto, G.; Pascarelli, S.; Boscherini, F.; Lamberti, C. et al. *Phys. Rev. B* **1998**, *57*, 14619-14622.

(87) Pöppl, A.; Kunz, S.; Himsl, D.; Hartmann, M. *J. Phys. Chem. C* **2008**, *112*, 2678-2684.

(88) Jee, B.; Eisinger, K.; Gul-E-Noor, F.; Bertmer, M.; Hartmann, M.; Himsl, D.; Poppl, A. *J. Phys. Chem. C* **2010**, *114*, 16630-16639.

(89) Jee, B.; Koch, K.; Moschkowitz, L.; Himsl, D.; Hartman, M.; Poppl, A. *J. Phys. Chem. Lett.* **2011**, *2*, 357-361.

(90) Gul-E-Noor, F.; Jee, B.; Poppl, A.; Hartmann, M.; Himsl, D.; Bertmer, M. *Phys. Chem. Chem. Phys.* **2011**, *13*, 7783-7788.

(91) Pöppl, A.; Kevan, L. *J. Phys. Chem.* **1996**, *100*, 3387-3394.

(92) Atherton, N. M.; Horsewill, A. J.; Volume 37, N., , pp. (13) *Mol. Phys.* **1979**, *37*, 1349-1361.

(93) Jang, H. J.; Hall, W. K.; d'Itri, J. L. *J. Phys. Chem.* **1996**, *100*, 9416-9420.

(94) Larsen, S. C.; Aylor, A.; Bell, A. T.; Reimer, J. A. *J. Phys. Chem.* **1994**, *98*, 11533-11540.

(95) Lo Jacono, M.; Fierro, G.; Dragone, R.; Feng, X. B.; dItri, J.; Hall, W. K. *J. Phys. Chem. B* **1997**, *101*, 1979-1984.